https://doi.org/10.1016/j.scib.2018.12.008

Rh-doped PdAg Nanoparticles as Efficient Methanol Tolerance Electrocatalytic Materials for Oxygen Reduction

Yingjun Sun[a,b#], Bolong Huang[c#], Nuoyan Xu[a], Yingjie Li[a], Mingchuan Luo[a], Chunji Li[a], Yingnan Qin[a,b], Lei Wang[b] and Shaojun Guo[a,d,e]*

[a]Department of Materials Science & Engineering, College of Engineering, Peking University, Beijing, 100871, China.

[b]College of Chemistry and Molecular Engineering, Qingdao University of Science and Technology, Qingdao 266042, China.

[c]Department of Applied Biology and Chemical Technology, The Hong Kong Polytechnic University, Hung Hom, Kowloon 999077, Hong Kong SAR.

[d]BIC-ESAT, College of Engineering, Peking University, Beijing, 100871, China.

[e]Department of Energy and Resources Engineering, College of Engineering, Peking University, Beijing, 100871, China.

[#]These authors contributed equally

*E-mail: guosj@pku.edu.cn

ABSTRACT

Direct methanol fuel cells (DMFCs) have received extensive attentions on their high efficiency, high reliability and no carbon emission. Unfortunately, the poor methanol tolerance and sluggish oxygen reduction reaction (ORR) at cathode have seriously hindered their further development. Herein we report the synthesis of a new class of Rh-doped PdAg alloy nanoparticles (NPs) for boosting ORR activity with high methanol tolerance capacity concurrently. The ORR mass activity of typical $Rh_4Pd_{40}Ag_{56}$ NPs is 4.2 times higher than that of commercial Pt catalyst. Moreover, it shows a great methanol tolerance capability by maintaining 92.4 % in ORR mass activity in alkaline solution with 0.1 mol L^{-1} methanol, against a big decrease of almost 100% for commercial Pt. Even after 30,000 potential cycles with 1.0 mol L^{-1} methanol, $Rh_4Pd_{40}Ag_{56}$ NPs still retain ORR mass activity of up to 68.3%. DFT calculations reveal that excellent ORR performance with excellent methanol tolerance

originates the active d-band-pinning engineering for an efficient site-independent electron-transfer. A generalized d-band mediated fine electron-transfer tuning path has blueprinted for effectively minimizing intrinsic ORR barriers with high current density. The present work highlights the key role of Rh doping in enhancing the ORR activity and methanol tolerance ability of PdAg NPs for future high-performance DMFCs.

Keywords: Rh-doped; multimetallic; oxygen reduction; methanol tolerance; fuel cells

1. Introduction

To meet the rising demand for energy and reduce the dependence on environmentally unfriendly fossil fuels, the exploration of new efficient energy conversion devices is highly attractive [1], [2], [3], [4], [5], [6], [7]. Direct methanol fuel cells (DMFCs) excel as an ideal solution for energy conversion [8], due to their high reliability, high efficiency and low carbon emission [9]. However, the development is greatly impeded by slow reaction kinetics of oxygen reduction reaction (ORR) and the poor methanol tolerance capacity caused by methanol permeation at cathode [10], [11], [12]. Precious platinum (Pt), as the most efficient metal for ORR, is commonly required [13], [14], [15]. Great efforts have been devoted to enhance the ORR activity of Pt-based multimetallic catalysts by designing hollow [16], [17], [18], alloy [19], [20], [21] and core/shell nanostructures [22], [23], [24], with interesting ligand [25], [26], ensemble [27], crystal facet [2], [28], [29] and strain effects [30], [31]. However, because of the methanol crossover [32], the methanol oxidation reaction (MOR) occurs at the cathode [33] and CO intermediates are easily absorbed onto Pt-based surface [34], which results in the CH3OH-poisoning [35], [36]. What's worse, it brings out a significant degradation of ORR performance and thereby a lower fuel efficiency [37], [38]. In this regards, developing alkaline based non-Pt catalyst with catalytic power comparable to or even superior to that of Pt and good methanol tolerance capability is highly desirable, *yet* a great challenge.

Palladium (Pd), as one of the promising alternative to Pt [39], has been explored by modifying their electronic and geometric structures for both the anode and cathode of DMFCs due to its relative good catalytic performance [40], [41], [42], [43], [44], [45]. However, for the reported Pd-based materials, it is still very difficult to simultaneously satisfy the following three key features for

DMFCs: excellent ORR activity, good methanol tolerance and excellent durability. We herein report a new class of Rh-doped PdAg NPs for achieving high ORR performance superior to Pt and good methanol tolerance capacity. The ORR mass activity of the as-made $Rh_4Pd_{40}Ag_{56}$ NPs can reach 0.50 A mg^{-1}, which is 3.8 times higher than that of $Pd_{45}Ag_{55}$ NPs catalyst. Furthermore, we find that $Rh_4Pd_{40}Ag_{56}$ NPs exhibit a prominent methanol tolerance capacity and durability, by maintaining 68.3% ORR mass activity after 30,000 potential cycles in an O_2-saturated 0.1 mol L^{-1} KOH solution with 1.0 mol L^{-1} methanol. While under the same condition, the ORR mass activity of commercial Pt catalyst shows an obvious methanol oxidation reaction (MOR) behavior. DFT calculations have preliminarily unraveled a key mechanism for site-independent d-band-pinning engineering towards highly efficient electron-transfer to Pd^0. Within this fine tuning path, our chosen precious metal (Rh) behaves as the active d-orbital-bridge to stably pin the Pd-4d band at lower position for reserving Pd^0. Throughout the tuned d-electron downshifting potential trend, the ORR intrinsic barriers have been alleviated, which robustly preserves the adsorbing O_2^{2-} and excludes the CH_3OH oxidizing adsorption *via* contrasted energetic competition. Meanwhile, with increasing the methanol content in KOH solution, the higher the silver content is, the more slowly the ORR mass activity of Rh-doped PdAg NPs decays, by comparing the Rh-doped PdAg NPs with different Pd/Ag atomic ratios. Our studies offer a feasible route to design and synthesize highly active non-Pt catalysts for ORR with a strong methanol-tolerant capability in alkaline solutions.

2. Materials and methods

2.1 Chemicals

Palladium(II) acetylacetonate ($Pd(acac)_2$, 99%), rhodium(III) acetylacetonate ($Rh(acac)_3$, 97 %), silver acetate ($C_2H_3AgO_2$, 99%), hexadecyl trimethyl ammonium bromide (CTAB, 99%), tungsten hexacarbonyl ($W(CO)_6$, 97%), oleylamine ($C_{18}H_{37}N$, OAm, > 70%), oleic acid ($C_{18}H_{34}O_2$, OA, > 85%) and Nafion (5%) were all purchased from Sigma-Aldrich. Commercial Pt (20 wt % Pt nanoparticles with an average size of 2~3 nm on Vulcan XC-72 carbon) was purchased from Johnson Matthey Corporation. Glucose ($C_6H_{12}O_6 \cdot H_2O$, analytical reagent), potassium hydroxide (KOH, analytical reagent, ≥ 85%), cyclohexane (C_6H_{12}, analytical reagent, ≥ 99.5%), methanol (CH_4O, analytical reagent, ≥ 99.7%), ethanol (C_2H_6O, analytical reagent, ≥ 99.7%) and isopropanol

(C_3H_8O, analytical reagent, ≥ 99.7%) were obtained from Beijing Tongguang Fine Chemicals Company. All the chemicals were used as received without further purification. The water (18 MΩ/cm) used in all experiments was prepared by passing through an ultra-pure purification system.

2.2 Instrumentation

Transmission electron microcopy (TEM) images were taken using a Tecani-G2 T20 at an acceleration voltage of 200 kV. X-ray diffraction (XRD) characterization was performed using an X'Pert-Pro X-ray powder diffractometer equipped with a Cu radiation source (λ = 0.15406 nm). To prepare the samples, the nanoparticles dispersed in cyclohexane were dropped onto the carbon-coated copper TEM grids using pipettes and dried under ambient condition for 5 min. The concentration of each catalyst was determined by the inductively coupled plasma atomic emission spectroscopy (ICP-AES, Agilent 8800). With the aid of sonication in ethanol, after the stability tests, the samples were scratched off from the electrode and collected for further TEM characterization.

2.3 Synthesis of Rh-doped PdAg NPs

In a typical synthesis of $Rh_4Pd_{40}Ag_{56}$ NPs, 8.0 mg of $Pd(acac)_2$, 6.0 mg of silver acetate, 2.0 mg of $Rh(acac)_3$, 10.0 mg of $W(CO)_6$, 40.0 mg of CTAB, 4.5 mL of OAm and 0.5 mL OA were added into a vial (volume: 20 mL). After the vial had been capped, the mixture was ultrasonicated for around 120 min to enable complete dissolution and yield a transparent solution. The vial was then transferred into an oil bath at a temperature of 180 ºC and maintained at this temperature for 3 h before it was cooled down to room temperature. The $Rh_4Pd_{40}Ag_{56}$ NPs were collected by centrifugation (8000 rpm, 5 min) and washed three times with an ethanol/cyclohexane (V/V = 1/1) mixture. After washing, the obtained nanoparticles were dispersed in cyclohexane for further use.

The $Pd_{45}Ag_{55}$ NPs were obtained by using the standard procedure except for the absence of Rh precursors. The syntheses of $Rh_4Pd_{50}Ag_{46}$ NPs and $Rh_4Pd_{32}Ag_{64}$ NPs were conducted by changing the amount of silver acetate from 6.0 mg to 3.0 mg and 12.0 mg, respectively, and keeping other conditions unchanged.

2.4 Preparation of carbon supported Rh-doped PdAg NPs catalysts

To prepare Rh-doped PdAg NPs/C catalyst, the as-synthesized Rh-doped PdAg NPs and Ketjen Black-300J carbon (10 mg) dispersed in 10 mL of ethanol and 10 mL of cyclohexane were mixed

under sonication for 2 h and collected by centrifugation. Then, the remained organic surfactants on nanocrystals were removed by being subject to thermal annealing at 200 ºC for 1 h in air.

2.5 Electrochemical measurements

The electrochemical measurements were conducted on a CHI760e electrochemical Workstation (Shanghai Chenhua Instrument Corporation, China) in a three-compartment cell. A glassy carbon Rotating Disk Electrode (RDE, diameter: 5 mm, area: 0.196 cm^2), a platinum plate and a saturated calomel electrode (SCE) were used as working, counter and reference electrodes, respectively. To prepare the 1.0 mg/mL catalyst ink, the catalysts were dispersed in a mixture of ultrapure water, isopropanol and Nafion solution (v:v:v =1:1:0.0025), and ultrasonicated for 30 minutes. Then, certain amount of the prepared catalyst ink was dropped onto the surface of RDE, yielding Pd loading of 10 μg/cm^2geo and 7.5μg /cm^2_{geo} for the commercial Pt/C and Rh-doped PdAg NPs/C catalysts. Cyclic voltammograms (CVs) were conducted in 0.1 mol L^{-1} KOH solution purged with saturated N_2 at a scan rate of 50 mV/s. To analyze the methanol tolerance capacity and durability of Rh-doped PdAg NPs for ORR, we carried out ORR tests in O_2-saturated 0.1 mol L^{-1} KOH solutions containing 0, 0.1, 0.5, and 1.0 mol L^{-1} methanol, respectively, using a rotating-disk electrode (RDE) at a rotation rate of 1600 rpm and a scan rate of 20 mV s^{-1}. The accelerated durability tests (ADTs) were performed in O_2-saturated 0.1 mol L^{-1} KOH containing 1 mol L^{-1} methanol solution by conducting CVs between 0.6 V and 1.1 V *versus* RHE for 30,000 potential cycles.

2.6 DFT models and calculations

We choose the CASTEP code with rotationally invariant (Anisimov type) DFT+U functional. The $Pd_{54}Ag_{54}$ (symmetry: *P4/mmm*) surface model was built with six-layer thick and atomic size of 108 atoms (*i.e.* $Pd_{54}Ag_{54}$ in 3×3×1 supercell) containing vacuum thickness of 12 Å. For the Rh-doped PdAg model (Rh-PdAg), we firstly choose the Pd-substituted Rh-doping with the size of $Rh_4Pd_{50}Ag_{54}$. Only the lattices in the top two layers are allowed to be freely relaxed. The Monkhost-Pack reciprocal space integration was performed using the mesh of 2×2×1 with Gamma-center-off, which was self-consistently selected for total energy minimization. With these special *k*-points, the total energy is converged to less than $5.0x10^{-7}$ eV *per* atom. The Hellmann-Feynman forces on the atom were converged to less than 0.001 eV/Å.

The geometry optimization has been performed with the algorithm of Broyden-Fletcher-Goldfarb-Shannon (BFGS). The PBE+U functional was chosen with a kinetic cutoff energy of 750 eV, with the valence electron states expressed in a plane-wave basis set. The ensemble DFT (EDFT) method of Marzari *et al* is used for improving convergence on the Pd and Rh transition metal contained compounds. The Hubbard U parameter self-consistently determined for the Pd-4d, Ag-4d, and Rh-4d orbitals by our new linear response method. This method has been already successfully reflecting the on-site orbital Coulomb potential for the transition metal and rare earth elements within DFT+U. The Pd, Ag, and Rh norm-conserving pseudopotentials are generated by OPIUM code based on the Kleinman-Bylander projector form, together with the non-linear partial core correction and a scalar relativistic averaging scheme. These treatments are used for averaging the spin-orbital coupling effect. We chose the (4*d,* 5*s*, 5*p*) states as the valence states. The RRKJ method is chosen for the optimization of the pseudopotentials. The Hubbard U parameters on the 4d orbitals are self-consistently to be U_d=4.04 eV, U_d=5.57 eV , and U_d=4.21 eV for Pd, Ag, and Rh respectively.

3. Results and discussion

A facile wet-chemical approach was used to synthesize Rh-doped PdAg NPs by using palladium(II) acetylacetonate ($Pd(acac)_2$), silver acetate, rhodium(III) acetylacetonate ($Rh(acac)_3$) as the metal precursors, tungsten hexacarbonyl ($W(CO)_6$) as the reducing agent, cetyltrimethyl ammonium bromide (CTAB) as the surfactant, oleic acid (OA) and oleylamine (OAm) as the solvents (Supporting Information). The mixture was heated to 180 ºC for 3 h in an oil bath. The optimal results show that the synthesis of Rh-doped PdAg NPs is highly controlled by the amount of $W(CO)_6$ and CTAB (**Fig. S1&S2**). The absence of $W(CO)_6$ or CTAB led to the formation of the irregular NPs.

Transmission electron microscopy (TEM) was used to characterize the morphology of the Rh-doped PdAg NPs. **Fig. 1a&1b** show the as-made NPs are in high purity and uniformity. The average size of NPs was 9.4 nm (**Fig. S3**). The TEM energy-dispersive X-ray spectroscopy (TEM-EDS) analysis in **Fig. 1c** reveals the composition of Rh/Pd/Ag is 4.3/41.8/53.9, being in accordance with the result from inductively coupled plasma-atomic emission spectroscopy (ICP-AES)

(Rh/Pd/Ag≈4/40/56). The Rh-doped PdAg NPs have a face-centered cubic (*fcc*) structure, proved by the powder X-ray diffractions (PXRD) pattern. The peaks of $Rh_4Pd_{40}Ag_{56}$ NPs NPs are those between *fcc* Pd (JCPDS No. 46-1043) [46] and *fcc* Ag (JCPDS No. 04-0783) [47] (**Fig. 1d**), indicating the formation of alloys. **Fig. 1e** shows the high-resolution TEM (HRTEM) image of a single $Rh_4Pd_{40}Ag_{56}$ NP. The well-defined lattice fringe of $Rh_4Pd_{40}Ag_{56}$ NP is 0.235 nm, which is between (111) interplanar distance of *fcc*-Pd (0.2246 nm) and that of *fcc*-Ag (0.237 nm). The TEM-EDS elemental mapping of a typical single $Rh_4Pd_{40}Ag_{56}$ NP reveals a homogeneous distribution of Rh, Pd and Ag throughout the NP (**Fig. 1f**). In addition, the compositions of Rh-doped PdAg can be controlled by varying the molar ratio of $Pd(acac)_2$ and silver acetate, and are analyzed by ICP-AES. TEM images suggest that the as-made NPs have an average size of 9.2 nm for $Rh_4Pd_{50}Ag_{46}$ NPs (**Fig. S4a-c**) and 9.8 nm for $Rh_4Pd_{32}Ag_{64}$ NPs (**Fig. S4d-f**). The XRD of Rh-doped PdAg NPs with different Pd/Ag compositions show the shift from the peaks attributed to *fcc* Pd phase to those of *fcc* Ag one with the increasing Ag content (**Fig. S5**). For comparison, the PdAg NPs were synthesized by using the standard procedure without adding Rh precursor. The morphology and structural analysis reveal the as-prepared PdAg NPs have an average size of 9.3 nm (**Fig. S6**). The composition of Pd/Ag is determined to be 45/55 by the ICP. The main XRD diffraction peaks of $Pd_{45}Ag_{55}$ NPs have a slightly negative shift compared to those of $Rh_4Pd_{40}Ag_{56}$, further confirming the formation of Rh-doped PdAg alloys (**Fig. S7**).

To investigate the electrocatalytic effect of Rh element in PdAg NPs, the ORR measurements of $Rh_4Pd_{40}Ag_{56}$ NPs and $Pd_{45}Ag_{55}$ NPs were carried out at room temperature in an O_2-saturated 0.1 M KOH solution with a rotation rate of 1600 rpm, and a sweep rate of 20 mV s^{-1}. **Fig. 2a** compares the geometric area (0.196 cm^2) normalized polarization curves of $Rh_4Pd_{40}Ag_{56}$ NPs/C, $Pd_{45}Ag_{55}$ NPs/C and Pt/C for ORR. The half-wave potential ($E_{1/2}$) for $Rh_4Pd_{40}Ag_{56}$ NPs/C is 0.858 V *vs.* RHE, almost 28 mV and 13 mV more positive than those of $Pd_{45}Ag_{55}$ NPs/C (0.830) and commercial Pt/C (0.845 V), respectively, suggesting the doped Rh atoms are essential for enhancing ORR activity (**Fig. 2b**). In order to give quantitative comparison on the intrinsic ORR activity, the corresponding Tafel plots for various catalysts are shown in **Fig. 2c**. $Rh_4Pd_{40}Ag_{56}$ NPs/C shows a Tafel slope of 82.9 mV dec^{-1}, lower than those of $Pd_{45}Ag_{55}$ (110.3 mV dec^{-1}) and Pt/C (89.1 mV dec^{-1}), indicating its fast kinetics

towards ORR than the other two catalysts. The electron transfer number on $Rh_4Pd_{40}Ag_{56}$ NPs/C is determined to be ~4 using rotating ring disk electrode (**Fig. S8**), indicating that $Rh_4Pd_{40}Ag_{56}$ NPs favor a 4 e^- oxygen reduction process. After normalizing the activity against the amount of noble metals (Pt or Pd), the $Rh_4Pd_{40}Ag_{56}$ NPs/C shows an excellent mass activity of 0.50 mA mg^{-1} at 0.9 V *vs.* RHE, 4.2 and 3.8 times higher than those of commercial Pt/C and $Pd_{45}Ag_{55}$, respectively (**Fig. 2d**). Comparison studies reveal that Rh doping plays an essential role in enhancing the ORR activity of Rh-doped PdAg NPs.

To evaluate the methanol tolerance capacity of Rh-doped PdAg NPs catalysts, we firstly measured the ORR activities of commercial Pt/C, Pd_{45}/Ag_{55} NPs/C and $Rh_4Pd_{40}Ag_{56}$ NPs/C in an O_2-saturated 0.1 mol L^{-1} KOH solution with 0.1 mol L^{-1} methanol (**Fig. 3a**). The $E_{1/2}$ of $Rh_4Pd_{40}Ag_{56}$ NPs/C catalyst only reveals a negative shift of 4 mV. However, under the same condition, the $Pd_{45}Ag_{55}$ NPs/C shows a shift of 29 mV, while the commercial Pt/C shows obvious MOR behavior, indicating the methanol tolerance capacity of PdAg NPs can be promoted by doping Rh element. To further investigate the methanol-tolerance properties, the ORR polarization curves of $Rh_4Pd_{40}Ag_{56}$ NPs/C were then examined in KOH solutions containing various methanol concentrations (**Fig. 3b**). With increasing the methanol content, the $E_{1/2}$ of $Rh_4Pd_{40}Ag_{56}$ NPs/C decays slowly, and its mass activity still can maintain 75.9% of original activity even through the methanol concentration reaches 1 M (**Fig. S9**). Furthermore, we performed the durability of the $Rh_4Pd_{40}Ag_{56}$ NPs/C using ADT under a sweep rate of 500 mV s^{-1} between 0.6 and 1.0 V *vs.* RHE in O_2-saturated 0.1 mol L^{-1} KOH solution containing 1 mol L^{-1}methanol. After 30,000 potential cycles, ORR polarization curves (**Fig. 3c**) and mass activity Tafel plot (in inset in Fig. 3c) show little shift, and the mass activity dropped by only 31.7% (**Fig. 3d**), suggesting good stability of $Rh_4Pd_{40}Ag_{56}$ NPs/C, which was proved by little change in morphology after durability tests (**Fig. S10**).

The Ag composition effect of the Rh-doped PdAg NPs on methanol tolerance for ORR was also investigated. **Fig. S11** shows the polarization curves of $Rh_4Pd_{50}Ag_{46}$ NPs/C and $Rh_4Pd_{32}Ag_{64}$ NPs/C in O_2-saturated 0.1 mol L^{-1} KOH solution with 0, 0.1, 0.5 and 1 mol L^{-1} methanol, respectively. When the solution without methanol, the $Rh_4Pd_{50}Ag_{46}$ NPs/C catalyst has the highest mass activity of 0.54 A mg^{-1} towards ORR, a little higher than $Rh_4Pd_{40}Ag_{56}$ NPs/C and 1.6 times than $Rh_4Pd_{32}Ag_{64}$

NPs/C (0.32 A mg^{-1}). However, as the methanol concentration increases to 1 mol L^{-1}, the $E_{1/2}$ drops by 41 mV for $Rh_4Pd_{50}Ag_{46}$ NPs/C, and 13 mV and 9 mV for $Rh_4Pd_{40}Ag_{56}$ NPs/C and $Rh_4Pd_{32}Ag_{64}$ NPs/C, respectively. The $Rh_4Pd_{50}Ag_{46}$ NPs/C descends most quickly compared with the other two (**Fig. 3e**). Although the $E_{1/2}$ declining value of $Rh_4Pd_{32}Ag_{64}$ NPs/C is least, it initial mass activity is much lower than $Rh_4Pd_{40}Ag_{56}$ NPs/C (**Fig. 3f** & *inset* of **Fig. 3f**). By analyzing the changing trend of $E_{1/2}$ and mass activity of commercial Pt/C, PdAg NPs and Rh-doped PdAg NPs (**Fig. 3**), we can draw conclusions as follows: i) Doping Rh atoms in PdAg NPs can efficient enhance the methanol tolerance towards ORR performance. ii) Appropriate silver content in Rh-doped PdAg NPs is important for ORR methanol tolerance. Excessive silver content in alloys is negative for ORR performance but can avoid methanol poisoning.

To further understand the mechanism of the enhanced activity and methanol tolerance of Rh-doped PdAg NPs, we reasoned the high performance of ORR catalysis and efficient methanol tolerance on the basis of first-principles DFT calculations. The PdAg (111) surface has been built-up (**Fig. 4a**). The Rh-doping has been preliminarily tried based on the Pd-substituted doping model (Rh_{Pd}) on the (111) surface (**Fig. 4b**). The bonding (filled-states) and anti-bonding (empty-states) of the electrons near the Fermi level (E_F) have been shown with the 3D real-space local orbital contour plots (**Fig. 4c and d**). For the PdAg surface, the HOMO and LUMO orbitals have been individually isolated with periodic array arrangement (**Fig. 4c**), showing a difficult electron transfer with site-to-site hopping barriers. While with the Rh-doping, the surface electronic states have been evidently modified. The electronic states are no longer symmetrically arranged, indicating a wider range of electron-rich area (**Fig. 4d**). This largely enhances the electron transfer between the surface and adsorbing initial reactants (*i.e.* O_2 and H_2O). These characters on the orbital contrast may contribute a good desorption efficiency.

We follow-up the d-band variation behavior by the projected partial density of states (PDOSs) calculations (**Fig. 4e**). From the PdAg to Rh-PdAg surface, the 4d-band centers of both surface Pd and Ag sites have uniformly been downshifted towards more electron-rich character. Namely, the 4d-band center of the Pd sites moves deeper from E_V-0.7 eV to E_V-1.2 eV (peak shifts 0.3 eV) where E_V=0 for E_F. The shifting behavior gets even more obvious for the Ag-sites from E_V-3.3 eV to E_V-4.3

eV (peak shift of 0.5 eV). Meanwhile, we find the Rh-4d-band possesses richer d-orbital levels bridging electronic states between the Ag and Pd. This indicates the lowered energetic barrier of electron transfer from Ag to Pd for producing the Pd^0 surface state and potentially less over-binding effect between Pd and reactant/intermediates. Further on the p-d coupling induced electron-transfer, we compared the 2p-band variations with influence of with and without Rh-doping. We find that the electron-transfer is mainly caused by the band-overlapping between Ag-4d and H_2O-2p while the O_2-2p band is nearly fixed (**Fig. 4f**). The H_2O-2p band turns to be even deeper on Rh-PdAg, showing electron-richer character with shifting of -0.5 eV and deeper than O_2-2p (**Fig. 4g**). Therefore, the Rh-4d-band bridges the Pd-Ag transfer gap and suppresses the 2p-band center for efficient formation of [OH^-] from H_2O.

We carried out the energetic pathway of ORR and compared the methanol adsorptions (**Fig. 5a**). The initial oxygen adsorption is the key role in affecting the ORR activities. The formation energy tells this contrast of -0.74 eV and -1.95 eV for PdAg and Rh-doped PdAg, respectively. The energetic barrier of Rh-PdAg (1.38 eV) is lower than the one in PdAg (1.98 eV). The one of Rh-PdAg occurs at the formation from [*OOH+H_2O+OH^-+2e^-] to [*O+H_2O+2OH^-+2e^-], while the barrier for PdAg stays at the formation from [*OH+3OH^-+e^-] to [*O+H_2O+2OH^-+2e^-]. This arises because the water-splitting and electron-transfer to H_2O is weaker on the PdAg surface than that of Rh-doped PdAg. We further consider the influence of the standard electrode potential U under the alkaline condition. The Rh-PdAg shows a U-independent energetic barrier, denoting an intrinsic performance for the bond-cleavage of [*OOH^-] to [*O+OH^-], while the PdAg system shows even higher (2.38 eV) increased by 0.401 eV. We finally study the formation of [4OH^-], which is much more stable for Rh-PdAg (-4.06 eV) than PdAg (-2.48 eV) with -1.58 eV lowered. Therefore, the pathway on the Rh-doped PdAg is more energetically favorable. We also compared the chemical adsorption for CH_3OH (**Fig. 5a**). It is clearly shown an adsorption barrier at the positive level of +1.81 eV for Rh-PdAg with contrast of +2.90 eV, elucidating an efficient methanol tolerance of Rh-PdAg surface system during the four electron ORR catalysis process.

From the local structural evolutions (**Fig. 5b**), we show that the O=O can be stably located and diagonally aligned local (Rh-Ag-Pd-Ag) square lattice. This can well reserve the O=O bond so that

the cleavage will not occur too early away from dissociation into [OH^-] or [O^{2-}] *via* two-electron pathway instead. It is the prerequisite for generalized four-electron based ORR. Moreover, this also recalls that the electron transfer between Ag-4d (donating center) and Pd-4d (accepting center) is critical, which determines the charge transfer rate. The [OOH^-] intermediate can be well preserved by such (Rh-Ag-Pd-Ag) square lattice. We find that both O^{2-} and [OH^-] can be favorably adsorbed on the surface with the three-fold pyramid oxygen bonding connecting the (Rh-Pd-Ag) uniformly, indicating a generalized stabilization for the O-intermediate-species by the Rh-doping. By discussing the electronic properties and energetic pathways, we confirm that the Rh-doped PdAg surface can achieve both have high electronic activities of the ORR energetic performance and efficient methanol tolerance simultaneously.

4. Conclusions

In summary, we have successfully demonstrated a remarkable Rh-doped PdAg NPs ORR catalyst with both excellent ORR activity and methanol tolerance capability. Electrocatalytic measurements exhibit that the mass activity and ORR methanol tolerance of PdAg NPs can be effectively enhanced by substantially low dose of Rh-doping. Among three different compositions, the $Rh_4Pd_{40}Ag_{56}$ NPs show an optimal ORR activity and methanol tolerance performance. DFT calculations reveal that the chosen Rh possesses abundant 4d-orbital energy levels (acting as a bridge) connecting the Ag and Pd electronic state on the surface, producing the lowered energetic barrier of electron-transfer highly efficient adsorption and desorption by downshifting 4d-band centers. Such active d-orbital-bridge pins the Ag d-electron-transfer towards O-species and simultaneously blockades the CH_3OH oxidation with contrasted chemisorption barrier. Such precious metal d-band fine-tuning steadily preserves Pd^0 for further optimal adsorbing O_2^{2-} without O-cleavage. This work blueprints a generalized and effective d-band-pining engineering, which advances a prominent ORR catalysis with robust methanol tolerance. Our work highlights the essential role of Rh in obtaining high methanol tolerance capacity and tuning optimal composition of Rh-doped PdAg NPs.

Conflicts of interest

The authors declare no competing financial interest.

Corresponding Author

*E-mail: guosj@pku.edu.cn

Acknowledgments

This work was financially supported by the National Natural Science Foundation of China (NSFC) (No. 51671003), National Basic Research Program of China (No. 2017YFA0206701), the China Postdoctoral Science Foundation (No. 2017M620526 and No. 2017M620518), Open Project Foundation of State Key Laboratory of Chemical Resource Engineering, the start-up supports from Peking University and Young Thousand Talented Program.

References

[1] Wang D, Xin HL, Hovden R, et al. Structurally ordered intermetallic platinum–cobalt core–shell nanoparticles with enhanced activity and stability as oxygen reduction electrocatalysts. Nat Mater, 2013; 12: 81–87

[2] Cui C, Gan L, Heggen M, et al. Compositional segregation in shaped Pt alloy nanoparticles and their structural behaviour during electrocatalysis. Nat Mater, 2013; 12: 765–771

[3] Seselj N, Engelbrekt C, Ding Y, et al. Tailored electron transfer pathways in Au_{core}/Pt_{shell}–graphene nanocatalysts for fuel cells. Adv Energy Mater, 2018; 8: 1702609

[4] Mayrhofer KJJ, Arenz M. Log on for new catalysts. Nat Mater, 2009; 1: 518–519

[5] Debe MK. Electrocatalyst approaches and challenges for automotive fuel cells. Nature, 2012; 486: 43–51

[6] Shang L, Yu H, Huang X, et al. Well-dispersed ZIF-derived Co,N-Co-doped carbon nanoframes through mesoporous-silica-protected calcination as efficient oxygen reduction electrocatalysts. Adv Mater, 2016; 28:1668–1674

[7] Yu H, Shang L, Bian T, et al. Nitrogen-doped porous carbon nanosheets templated from g-C_3N_4 as metal-free electrocatalysts for efficient oxygen reduction reaction. Adv Mater, 2016; 28: 5080–5086

[8] Mehmood A, Scibioh MA, Prabhuram J, et al. A review on durability issues and restoration techniques in long-term operations of direct methanol fuel cells. J Power Sources, 2015; 297: 224–241

[9] Yue X, He C, Zhong C, et al. Fluorine‐doped and partially oxidized tantalum carbides as nonprecious metal electrocatalysts for methanol oxidation reaction in acidic media. Adv Mater, 2016; 28: 2163-2169

[10] Wang A-L, Xu H, Feng J-X, et al. Design of Pd/PdNi/Pd sandwich-structured nanotube array catalysts with special shape effects and synergistic effects for ethanol electrooxidation. J Am Chem Soc, 2013; 135: 10703-10709

[11] Xu C, Wang H, Shen PK, et al. Highly ordered Pd nanowire arrays as effective electrocatalysts for ethanol oxidation in direct alcohol fuel cells. Adv Mater, 2007; 19: 4256-4259

[12] Gao MR, Gao Q, Jiang J, et al. A methanol‐tolerant Pt/$CoSe_2$ nanobelt cathode catalyst for direct methanol fuel cells. Angew Chem Int Ed, 2011; 123: 5007-5010

[13] Huang X, Zhao Z, Cao L, et al. High-performance transition metal–doped Pt_3Ni octahedra for oxygen reduction reaction. Science, 2015; 348: 1230-1234

[14] Snyder J, Livi K, Erlebacher J. Oxygen reduction reaction performance of [mtbd][beti]‐encapsulated nanoporous NiPt alloy nanoparticles. Adv Funct Mater, 2013; 23: 5494-5501

[15] Luo M, Sun Y, Zhang X, et al. Stable high‐index faceted Pt skin on zigzag‐like ptfe nanowires enhances oxygen reduction catalysis. Adv Mater, 2018; 30: 1705515

[16] Chen C, Kang Y, Huo Z, et al. Highly crystalline multimetallic nanoframes with three-dimensional electrocatalytic surfaces. Science, 2014; 343: 1339-1343

[17] Xia BY, Wu HB, Wang X, et al. One-pot synthesis of cubic $PtCu_3$ nanocages with enhanced electrocatalytic activity for the methanol oxidation reaction. J Am Chem Soc, 2012; 134: 13934-13937

[18] Luo S, Tang M, Shen PK, et al. Atomic‐scale preparation of octopod nanoframes with high‐index facets as highly active and stable catalysts. Adv Mater, 2017; 29:

[19] Li M, Zhao Z, Cheng T, et al. Ultrafine jagged platinum nanowires enable ultrahigh mass activity for the oxygen reduction reaction. Science, 2016; 354: 1414-1419

[20] Bu L, Ding J, Yao J, et al. A general method for multimetallic platinum alloy nanowires as highly active and stable oxygen reduction catalysts. Adv Mater, 2015; 27: 7204–7204

[21] Zhang C, Sandorf W, Peng Z. Octahedral Pt_2CuNi uniform alloy nanoparticle catalyst with high activity and promising stability for oxygen reduction reaction. ACS Catal, 2015; 5: 2296-2300

[22] Bu L, Zhang N, Guo S, et al. Biaxially strained PtPb/Pt core/shell nanoplate boosts oxygen reduction catalysis. Science, 2016; 354: 1410-1414

[23] Cai B, Hübner R, Sasaki K, et al. Core–shell structuring of pure metallic aerogels towards highly efficient platinum utilization for the oxygen reduction reaction. Angew Chem Int Ed, 2018; 57: 2963-2966

[24] Gan L, Heggen M, Rudi S, et al. Core–shell compositional fine structures of dealloyed Pt_xNi_{1-x} nanoparticles and their impact on oxygen reduction catalysis. Nano Lett, 2012; 12: 5423-5430

[25] Bu L, Guo S, Zhang X, et al. Surface engineering of hierarchical platinum-cobalt nanowires for efficient electrocatalysis. Nat Commun, 2016; 7: 11850

[26] Park J, Kanti Kabiraz M, Kwon H, et al. Radially phase segregated PtCu@ PtCuNi dendrite@ frame nanocatalyst for the oxygen reduction reaction. ACS nano, 2017; 11: 10844-10851

[27] Xin L, Yang F, Rasouli S, et al. Understanding Pt nanoparticle anchoring on graphene supports through surface functionalization. ACS Catal, 2016; 6: 2642-2653

[28] Stamenkovic VR, Fowler B, Mun BS, et al. Improved oxygen reduction activity on Pt_3Ni (111) via increased surface site availability. Science, 2007; 315: 493-497

[29] Huang X, Zhao Z, Chen Y, et al. A rational design of carbon-supported dispersive Pt-based octahedra as efficient oxygen reduction reaction catalysts. Energy Environ Sci, 2014; 7: 2957-2962

[30] Zhang S, Zhang X, Jiang G, et al. Tuning nanoparticle structure and surface strain for catalysis optimization. J Am Chem Soc, 2014; 136: 7734-7739

[31] Luo M, Guo S. Strain-controlled electrocatalysis on multimetallic nanomaterials. Nat Rev Mater, 2017; 2: 17059

[32] Argun AA, Ashcraft JN, Hammond PT. Highly conductive, methanol resistant polyelectrolyte multilayers. Adv Mater, 2008; 20: 1539-1543

[33] Cao X, Wang N, Han Y, et al. Ptag bimetallic nanowires: Facile synthesis and their use as excellent electrocatalysts toward low-cost fuel cells. Nano Energy, 2015; 12: 105-114

[34] Wen Z, Liu J, Li J. Core/shell Pt/C nanoparticles embedded in mesoporous carbon as a methanol‐tolerant cathode catalyst in direct methanol fuel cells. Adv Mater, 2008; 20: 743-747

[35] Kamiya K, Kamai R, Hashimoto K, et al. Platinum-modified covalent triazine frameworks hybridized with carbon nanoparticles as methanol-tolerant oxygen reduction electrocatalysts. Nat Commun, 2014; 5: 5040

[36] Ud Din MA, Saleem F, Ni B, et al. Porous tetrametallic ptcubimn nanosheets with a high catalytic activity and methanol tolerance limit for oxygen reduction reactions. Adv Mater, 2017; 29: 1604994

[37] Pan S, Cai Z, Duan Y, et al. Tungsten diselenide/porous carbon with sufficient active edge-sites as a Co-catalyst/Pt-support favoring excellent tolerance to methanol-crossover for oxygen reduction reaction in acidic medium. Appl Catal B Environ, 2017; 219: 18-29

[38] Mahmood A, Xie N, Din MAU, et al. Shape controlled synthesis of porous tetrametallic PtAgBiCo nanoplates as highly active and methanol-tolerant electrocatalyst for oxygen reduction reaction. Chem Sci, 2017; 8: 4292-4298

[39] Luo M, Sun Y, Qin Y, et al. Palladium-based nanoelectrocatalysts for renewable energy generation and conversion. Mater Today Nano, 2018;1: 29-40

[40] Jiang K, Wang P, Guo S, et al. Ordered PdCu‐based nanoparticles as bifunctional oxygen‐reduction and ethanol‐oxidation electrocatalysts. Angew Chem Int Ed, 2016; 55: 9030-9035

[41] Calderón Gómez JC, Moliner R, Lázaro MJ. Palladium-based catalysts as electrodes for direct methanol fuel cells: A last ten years review. Catalysts, 2016; 6: 130

[42] Wu H, Li H, Zhai Y, et al. Facile synthesis of free‐standing Pd‐based nanomembranes with enhanced catalytic performance for methanol/ethanol oxidation. Adv Mater, 2012; 24: 1594-1597

[43] Wang K, Qin Y, Lv F, et al. Intermetallic Pd_3Pb nanoplates enhance oxygen reduction catalysis with excellent methanol tolerance. Small Methods, 2018; 2: 1700331

[44] Xu Q, Chen W, Yan Y, et al. Multimetallic AuPd@Pd@Pt core-interlayer-shell icosahedral electrocatalysts for highly efficient oxygen reduction reaction. Science Bulletin, 2018; 63: 494-501

[45] Jiang G, Li X, Lv X, et al. Core/shell FePd/Pd catalyst with a superior activity to Pt in oxygen reduction reaction. Science Bulletin, 2016; 61: 1248-1254

[46] Sun Y, Zhang X, Luo M, et al. Ultrathin PtPd‐based nanorings with abundant step atoms enhance oxygen catalysis. Adv Mater, 2018; 1802136

[47] Liu M, Lu Y, Chen W. PdAg nanorings supported on graphene nanosheets: Highly methanol‐tolerant cathode electrocatalyst for alkaline fuel cells. Adv Funct Mater, 2013; 23: 1289-1296

Figures

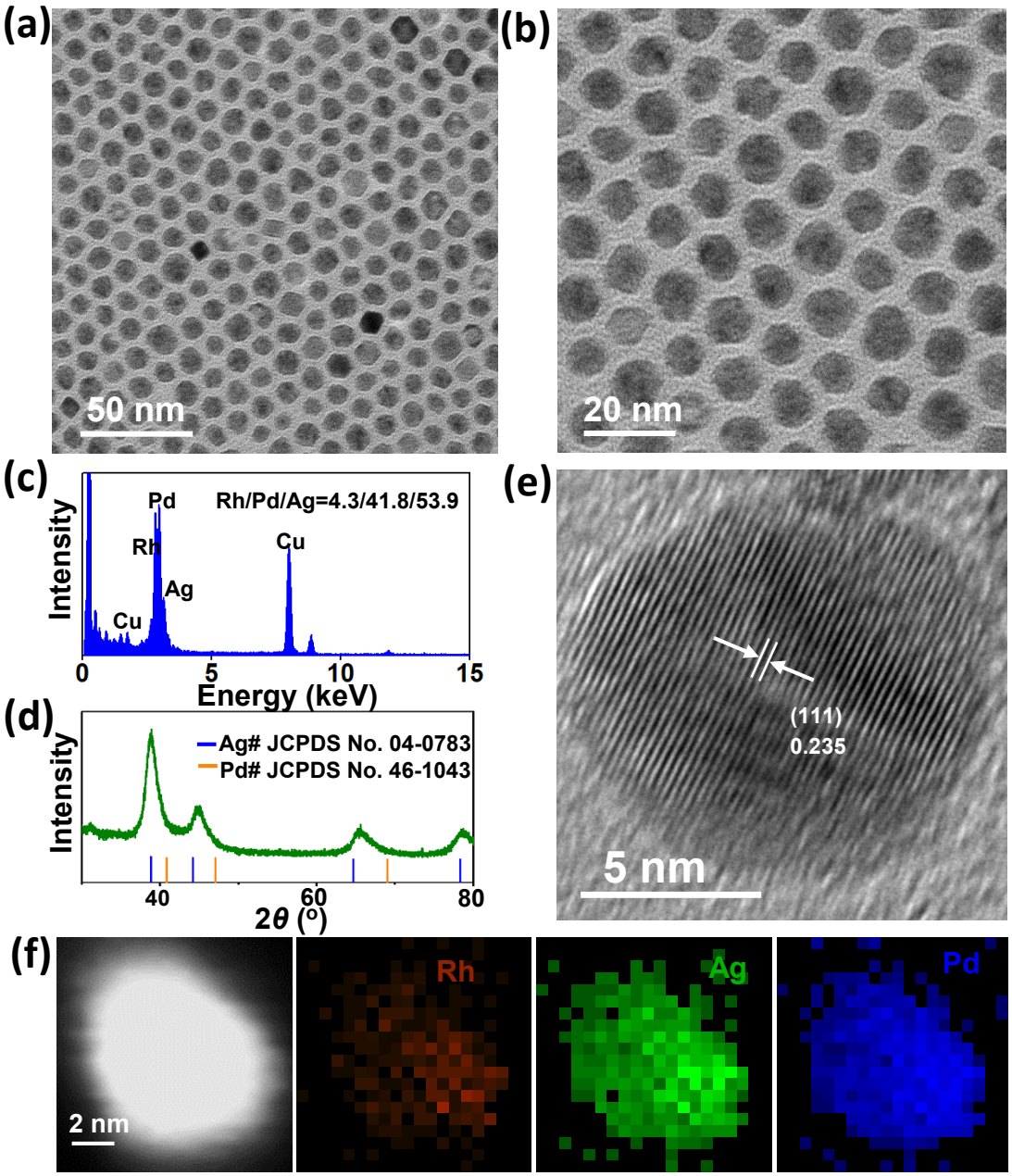

Fig. 1 | Morphology and structure characterization of $Rh_4Pd_{40}Ag_{56}$ NPs. (a, b) TEM images, **(c)** TEM-EDS spectrum, **(d)** PXRD pattern, **(e)** HRTEM image and (**f**) STEM-EDS elemental mapping of $Rh_4Pd_{40}Ag_{56}$ NPs.

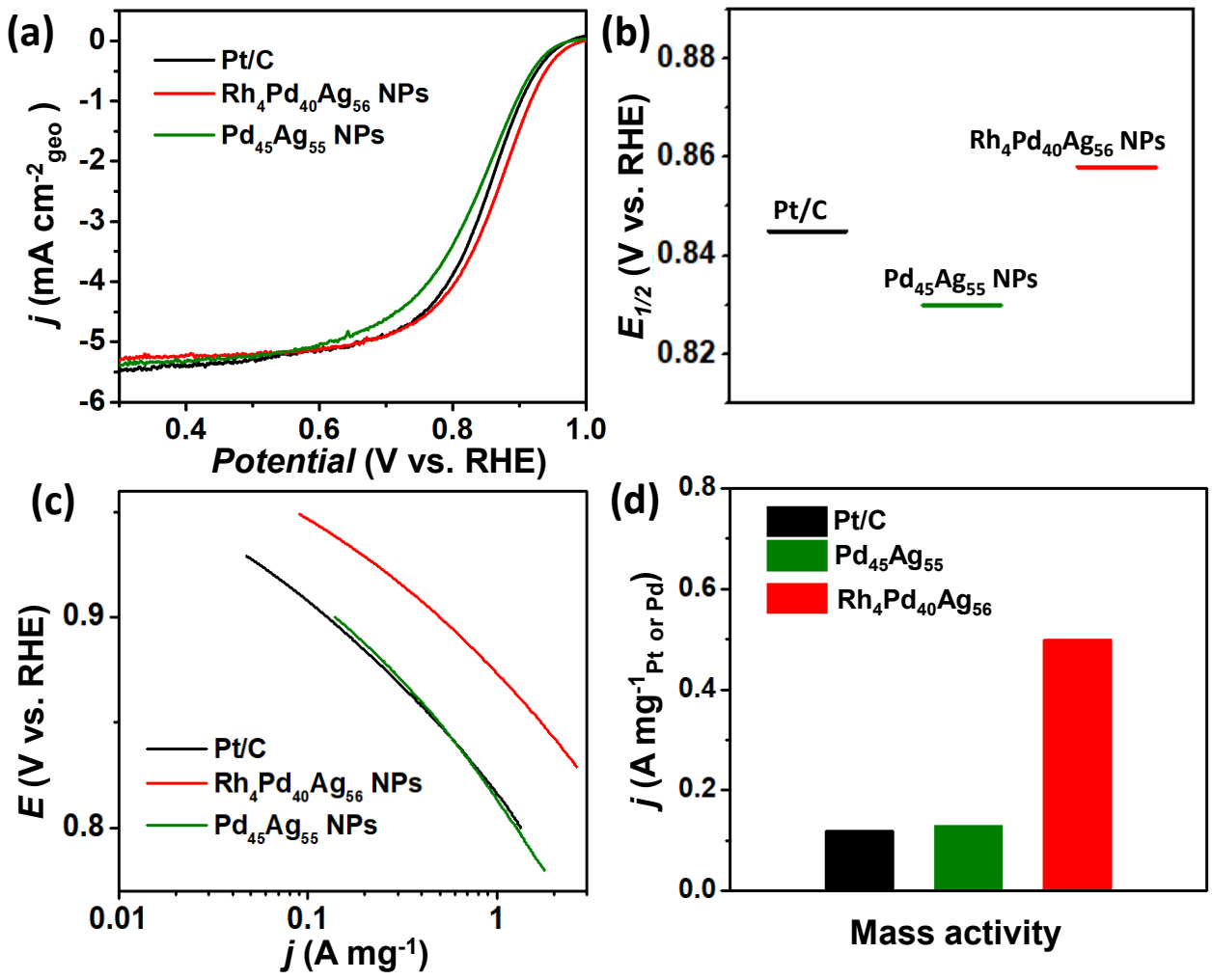

Fig. 2 | Comparison of ORR activities of $Rh_4Pd_{40}Ag_{56}$ NPs, $Pd_{45}Ag_{55}$ NPs and commercial Pt/C electrocatalysts. (a) ORR polarization curves, (b) half-wave potential ($E_{1/2}$) values, (c) Tafel plots, and (d) histogram of mass activities of various catalysts. Polarization curves were recorded at room temperature in O_2-saturated 0.1 mol L^{-1} KOH solutions. Scan rate: 20 mV/s. Rotation rate: 1600 rpm.

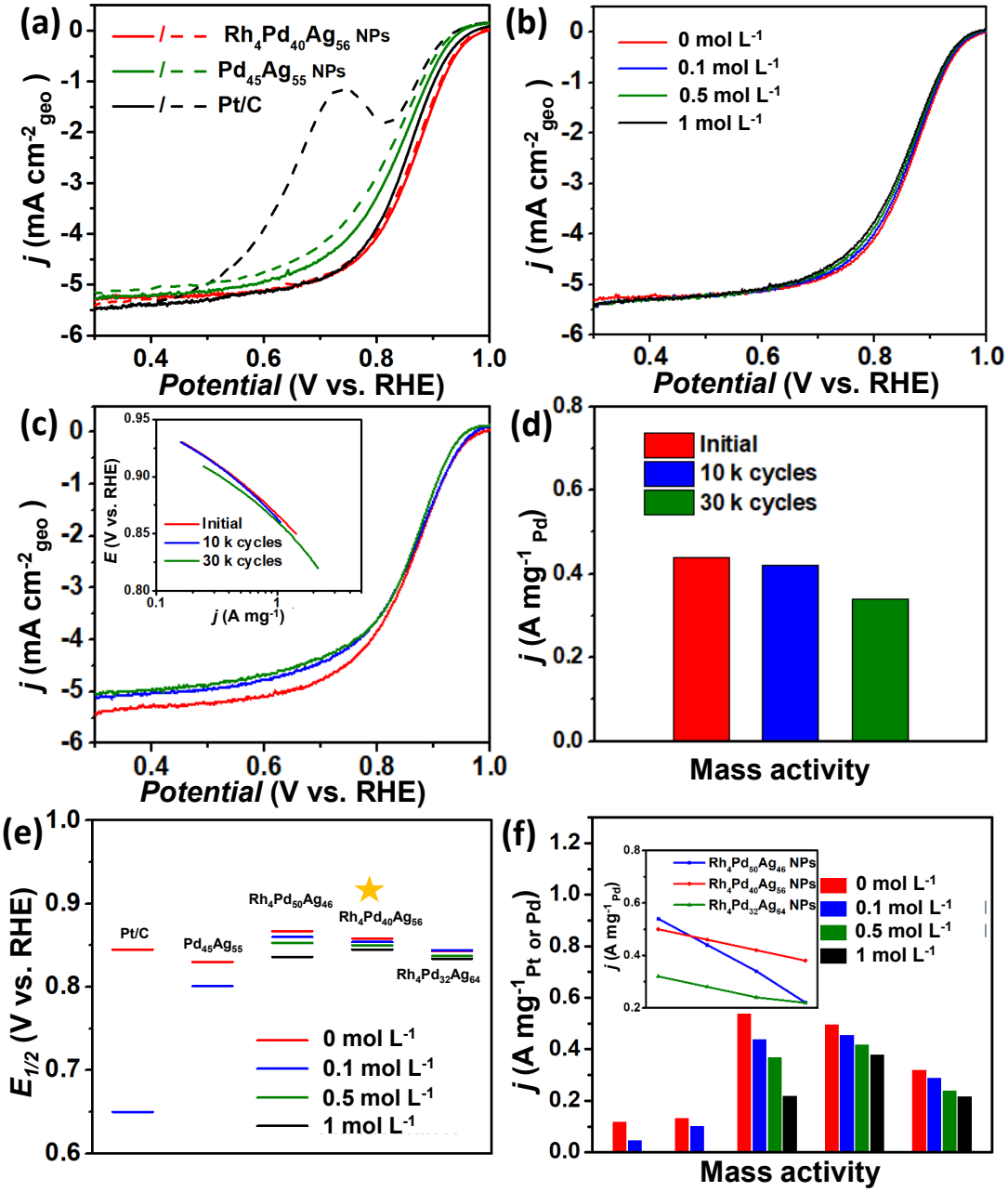

Fig. 3 | Evaluation of the methanol tolerance capacity and durability of the electrocatalysts. (a) ORR polarization curves of $Pd_{45}Ag_{55}$ NPs, $Rh_4Pd_{40}Ag_{56}$ NPs and commercial Pt/C in O_2-saturated 0.1 mol L^{-1} KOH solutions with (dashed lines) and without (solid lines) 0.1 mol L^{-1} methanol. **(b)** ORR polarization curves of $Rh_4Pd_{40}Ag_{56}$ NPs in O_2-saturated 0.1 mol L^{-1} KOH solutions with successive methanol concentration (0, 0.1, 0.5, 1 mol L^{-1}). **(c)** ORR polarization curves, and **(d)** histogram of ORR mass activity of $Rh_4Pd_{40}Ag_{56}$ NPs before and after 10,000, 30,000 potential cycles in 1 mol L^{-1} methanol solution. The *inset* in (c) is the Tafel plots of $Rh_4Pd_{40}Ag_{56}$ NPs before and after 10,000, 30,000 potential cycles **(e)** Half-wave potential ($E_{1/2}$) values and **(f)** ORR mass activity histograms of $Rh_4Pd_{50}Ag_{46}$ NPs, $Rh_4Pd_{40}Ag_{56}$ NPs, $Rh_4Pd_{32}Ag_{64}$ NPs, $Pd_{45}Ag_{55}$ NPs and commercial Pt before and after adding various methanol concentration (0.1, 0.5, 1 mol L^{-1}). The *inset* in (f) is mass activities line graph of Rh-doped PdAg NPs with different compositions before and after adding various methanol concentration (0.1, 0.5, 1 mol L^{-1}).

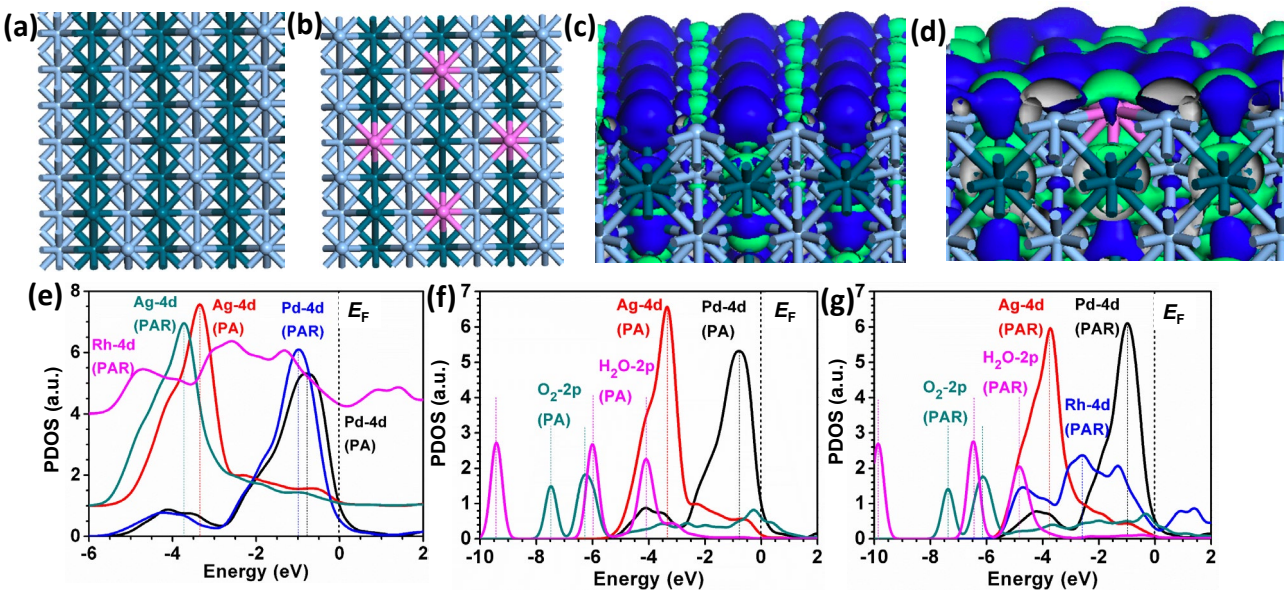

Fig. 4 | DFT calculations. (a) The atomic structure of PdAg surface model. **(b)** The structural model of Rh-doped PdAg surface. **(c)** The 3D contour plots of charge densities for both bonding and anti-bonding orbitals of PdAg surface. **(d)** The 3D contour plots of charge densities for both bonding and anti-bonding orbitals of Rh-doped PdAg surface. **(e)** The partial density of states (PDOS) of Pd-4d, Ag-4d and Rh-4d orbital levels within PdAg and Rh-doped PdAg surfaces. **(f)** The PDOSs of p-d band overlapping effect for O_2-2p, H_2O-2p, Pd-4d, Ag-4d and Rh-4d orbital levels on the PdAg surface. **(g)** The PDOSs of p-d band overlapping effect for O_2-2p, H_2O-2p, Pd-4d, Ag-4d and Rh-4d orbital levels on the Rh-PdAg surface. (Bonding orbital=blue surface, anti-bonding orbital=green surface, Pd=dark green, Ag=light blue, and Rh=pink).

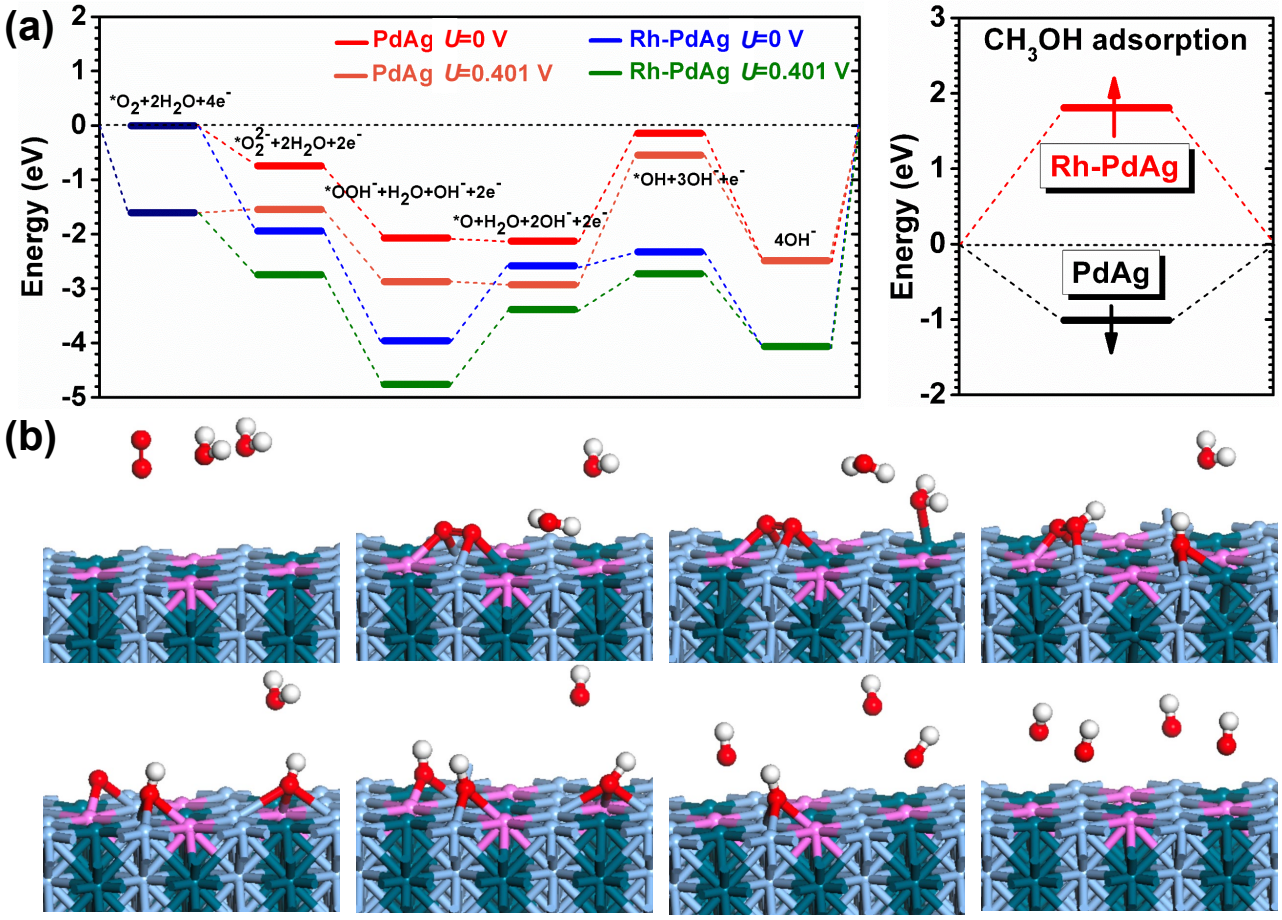

Fig. 5 | Energetic pathway of ORR and compared methanol adsorptions. (a) The free energy-level diagram of the catalytic ORR (four-electron) steps conducted on the PdAg and Rh-PdAg surfaces with consideration of both U=0 and U=0.401 V for the electrode potentials. The chemical adsorption of methanol on these two surfaces have been also given. (b) The local structures and bonding variations of $*O_2$, *OOH, *OH, and H_2O* in the simulation for interpreting the catalytic ORR mechanism on the Rh-PdAg system. (Pd=dark green, Ag=light blue, Rh=pink, O=red, and H=white).